



Drug loading capacity of microporous β -pyrophosphate crystals

A.D. Anastasiou^{a,*}, M. Nerantzaki^{b,c}, A.P. Brown^a, A. Jha^a, D.N. Bikiaris^c

^a School of Chemical and Process Engineering, University of Leeds, Leeds LS2 9JT, UK

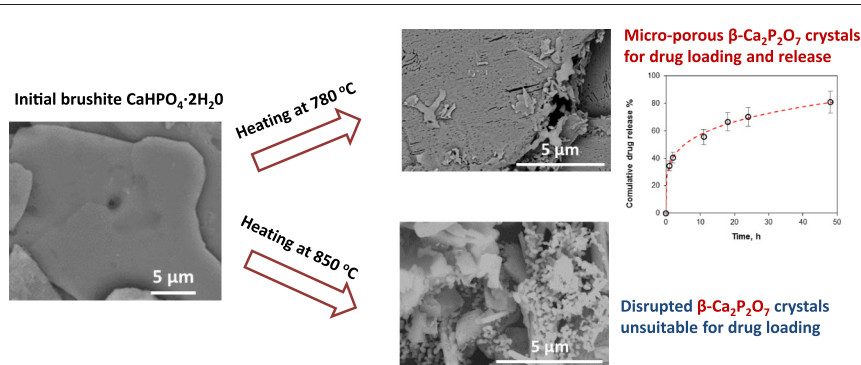
^b Sorbonne University, UPMC Univ Paris 06, CNRS, UMR 8234, PHENIX Laboratory, case 51, 4 place Jussieu, 75252 Paris cedex 05, France

^c Laboratory of Polymer Chemistry and Technology, Chemistry Department, Aristotle University of Thessaloniki, 54124 Thessaloniki, Greece

HIGHLIGHTS

- Heat treatment of brushite, results in the formation of microporous β -pyrophosphate.
- There is the capability to tailor microporosity for drug adsorption by controlled heat treatment conditions.
- β -pyrophosphate can be loaded with antibiotics for localised drug delivery.
- Potentially, β -pyrophosphate could be used for treating periodontitis or peri-implantitis.

GRAPHICAL ABSTRACT



ARTICLE INFO

Article history:

Received 10 October 2018

Received in revised form 12 February 2019

Accepted 13 February 2019

Available online 14 February 2019

Keywords:

Drug delivery
Chloramphenicol
Heat treatment
Mesoporous
 β -Pyrophosphate

ABSTRACT

Periodontitis and peri-implantitis are two characteristic examples where bacterial infections compromise the healing of dental tissues. Drug eluting scaffolds are a potential solution to this problem but their fabrication requires suitable biomaterials with significant drug loading capacity and regenerative potential to support new tissue formation. With this aim, porous β -pyrophosphate crystals having a micro-pore area of $2.59 \text{ m}^2/\text{g}$ and an average pore diameter of 65 nm, have been obtained by the heat treatment of brushite (at 780 °C). To demonstrate the drug loading potential of the mineral, experiments with chloramphenicol have been conducted. After tests with four common bacteria, the drug loaded mineral was shown to have enhanced antibacterial properties, particularly towards *E. coli* (74% growth inhibition) and *S. aureus* (48% growth inhibition). Taking into account β -pyrophosphate's significant role in hard tissue mineralisation and the capability to tailor crystal microporosity characteristics by controlled heat treatment, the mineral can be considered as an ideal biomaterial for localised drug delivery in dental applications.

Crown Copyright © 2019 Published by Elsevier Ltd. This is an open access article under the CC BY license (<http://creativecommons.org/licenses/by/4.0/>).

1. Introduction

Bacterial colonisation can have significant implications for the healing process of tissues. Two characteristic clinical conditions related to bacterial contamination, are periodontitis (PD) and peri-implantitis

(PI). PD is an inflammatory disease affecting the tissues that support teeth. The disease begins when bacterial growth on a tooth surface forms microbial plaque. An over-aggressive immune response against this, leads to chronic inflammation of the periodontal tissues and the destruction of the periodontal ligaments. If left untreated PD leads to tooth loss [1] and current evidence also associates PD with other systemic health conditions (e.g. cardiovascular diseases) [2]. Although at the moment there are many treatment options available (e.g. soft tissue grafts, bone replacement grafts, root modification, growth/

* Corresponding author.

E-mail addresses: a.anastasiou@leeds.ac.uk, a.anastasiou83@gmail.com (A.D. Anastasiou).

differentiation factors) most of them fail to provide restoration of periodontal tissues because of the oral bacterial which are attached to the tooth surface and contaminate any newly formed tissues [3–5]. PI on the other hand, is defined by infections around implants in orthopaedics and regenerative dentistry [6]. Epidemiological studies suggest that between 12% and 43% of dental implants will at some point develop symptoms of PI when in orthopaedics, and 2–5% of all implant related procedures are likely to be compromised by bacterial infections [7].

In order to mitigate the risk of infection and to provide effective treatment options to clinicians, researchers have focused their efforts on the development of materials and scaffolds with the potential to inhibit bacterial growth. To that end, different strategies have been pursued; porous materials (i.e. scaffolds and nanoparticles) with the potential to be loaded with and subsequently release drugs ([8–10]), surfaces with antibacterial properties ([11,12]) and biomaterials (e.g. calcium phosphates) doped with ions known for their antibacterial activity (e.g. Ag^+ , Ce^{3+}) [13,14]. Drug eluting scaffolds, for localised drug delivery during the entire cycle of healing, may be an effective option for dealing with the aforementioned clinical conditions. The critical step in this approach is the selection of a suitable biomaterial with significant drug loading capacity (for physical or chemical loading) and the regenerative potential to support new tissue formation. In contrast with well-known drug vehicles, which in most cases are polymeric nanoparticles with high resorption rates, this application requires materials with lower dissolution rates (matching the healing rate of the targeted tissue) in order to secure controlled drug delivery for longer time periods. Based on these criteria, calcium phosphate minerals are promising candidates for localised drug elution. Due to the structural and chemical similarity with the natural mineral of human hard tissues (i.e. carbonated hydroxyapatite), calcium phosphate biomaterials have been extensively investigated for tissue engineering applications like implant coatings, drug carrying vehicles, fabrication of scaffolds for bone regeneration etc. Hydroxyapatite [HAP: $\text{Ca}_{10}(\text{PO}_4)_6(\text{OH})_2$] is the most popular of the apatites in clinical practice, however its effectiveness as a bone graft material is disputable due to a number of factors like brittleness and the extremely low rate of bioresorption [15]. β -pyrophosphate (CPP: $\beta\text{-Ca}_2\text{P}_2\text{O}_7$) is a promising alternative grafting material with good osteoconductive activity and better biodegradation rates compared to HAP [16]. Recent studies demonstrate the importance of pyrophosphate ions to the mineralisation of bone (e.g. [17]). Grover et al. [15] suggested that enzymatic action accelerates dissolution of the inorganic pyrophosphate ions causing a simultaneous loss of mineralisation and localised rise in ion saturation and as a result the presence of pyrophosphate can stimulate bone mineralisation and healing. The mineral is biocompatible, non-toxic and found to have similar mechanical properties to dental enamel which makes it suitable for dental related applications (e.g. coating of dental implants) [18]. So far, most of the published research regarding β -pyrophosphate, has been focused on bioactivity and the regenerative potential of the mineral and to the best of our knowledge, little work has been presented for pyrophosphate as a drug delivery vehicle.

CPP crystals can be obtained by heat treatment of brushite (DCPD: $\text{CaHPO}_4 \cdot 2\text{H}_2\text{O}$) in a temperature range between 750 and 850 °C. As discussed in Anastasiou et al., [19], upon heating water is removed from the DCPD structure resulting in the formation of extended porosity at the surface of the final CPP crystals. The aim of the current work is to demonstrate the drug loading capacity of these porous pyrophosphate crystals and the potential use of the mineral as a localised drug delivery system. Chloramphenicol ($\text{C}_{11}\text{H}_{12}\text{Cl}_2\text{N}_2\text{O}_5$), a broad spectrum antibiotic appropriate for treating a number of bacterial infections like meningitis, has been used for the experiments. The model drug has a toxic effect on human mitochondria resulting in bone marrow suppression and in general, is inappropriate for tissue engineering applications. However, it was selected in this work as a demonstration drug because it is easy to identify by spectroscopic techniques (i.e. FTIR, UV-VIS) and EDX mapping (due to the Cl in its structure). The antibacterial properties of the

drug loaded minerals, were evaluated following exposure to four common bacteria i.e. *Escherichia coli*, *Staphylococcus aureus*, *Bacillus subtilis* and *Bacillus cereus*. The selection of the aforementioned bacteria was based on their response towards chloramphenicol in order to prove the release of the drug from the tested material i.e. is not directly relevant to treatment of PD or PI.

2. Materials and methods

The wet precipitation route that is described by Anastasiou et al., [18] was followed for the synthesis of the DCPD. 200 mL of a 0.1 M $\text{Ca}(\text{NO}_3)_2 \cdot 4\text{H}_2\text{O}$ aqueous solution was heated to 37 °C, then a 0.1 M $(\text{NH}_4)_3\text{PO}_4$ solution (200 mL) was added drop by drop. The final mixture was left under continuous stirring at 37 °C for 2 h, then left to settle for 1 h to allow precipitation. The DCPD crystals formed were collected on a filter paper (Whatman grade 44 with pores of 3 μm), washed several times with distilled water and dried for 24 h at 70 °C. For the preparation of monetite (DCP: Ca_2HPO_4), DCPD powder was heat treated for 2 h at 200 °C. Similarly, β -pyrophosphate (CPP1) was prepared by heating DCPD powder at 750 °C for 2 h.

To load the drug on mineral crystals the procedure described in [20] was followed. 42 mg of chloramphenicol was introduced to 300 mL of ultra-pure water and left to dissolve in an ultrasound bath for 40 min. For each mineral, 70 mg of the corresponding powder was added to a 100 mL flask and then filled with the dissolved drug solution resulting in an initial concentration of 200 μg of drug/mg of nanoparticles. The flasks were covered with aluminium foil to prevent any photo-induced reactions and placed on stirring plates to keep the crystals dispersed. To determine the percentage of the drug loaded onto the mineral particles, the drug concentration remaining in the solution was measured with a UV-VIS spectrometer (Perkin Elmer, LAMBDA 950) multiple times during the incubation period. Before sampling (every 24 h), the stirring was interrupted to allow the minerals to settle for 1 h and then 5 mL (for each sample) was removed with a pipette from the top layer of the solution. The samples were centrifuged for 20 min at 10,000 rpm (relative centrifugal force $\sim 11,000g$) in order to separate any mineral crystals and then filtered with Nylon syringe filters. The concentration of the drug in each solution was determined through spectroscopy measurements (UV-VIS) over a range of wavelengths between 200 and 400 nm, as described below. At the end of the drug loading period the mixture was left to settle for 1 h and the remaining solution was removed from the flask with a 100 mL pipette. The crystals of each mineral were collected in vials and frozen to -40 °C for 24 h, these were then freeze dried for 24 h to remove any moisture. The same procedure was repeated in order to load CPP1 crystals with a second drug, Doxycycline-hyclate (DOX) (CAS 24390-14-5, acquired by Sigma Aldrich) which is more appropriate for treating PD [21]. The CPP1 crystals loaded with DOX were tested for monitoring the cumulative drug release over a period of 48 h by UV-VIS spectrometer (Perkin Elmer, LAMBDA 950) measurement of the incubation solution (as per the loading measurements for the chloramphenicol). The as-synthesized and drug loaded materials used in the present work are summarised in Table 1.

Table 1
Minerals used and preparation method before drug loading.

Code	Description	Chemical formula	Synthesis
DCPD	Brushite	$\text{CaHPO}_4 \cdot 2\text{H}_2\text{O}$	Wet precipitation
D-DCPD	Drug loaded brushite	Ca:P ratio = 1	
DCP	Monetite	CaHPO_4	Heat treatment of brushite (200 °C, 2 h)
D-DCP	Drug loaded monetite	Ca:P ratio = 1	
CPP1	β -pyrophosphate	$\beta\text{-Ca}_2\text{P}_2\text{O}_7$	Heat treatment of brushite (780 °C 2 h)
D-CPP	Drug loaded β -pyrophosphate	Ca:P ratio = 1	

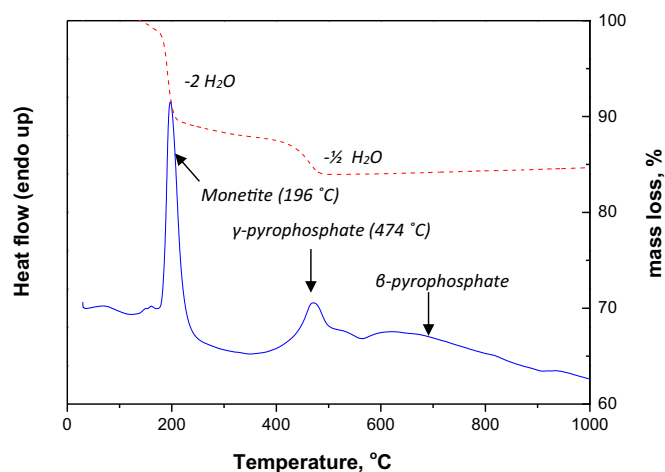


Fig. 1. STA analysis of the initial brushite (DCPD) and identification of the transformation temperatures (the DSC curve is in blue and values are shown on the left y-axis while the TGA curve is shown in red and values re-reported on the right y-axis).

The crystal structure and purity of the synthesized mineral phases were analysed by X-Ray powder diffraction using a Philips X'Pert MPD, with monochromatic Cu K α radiation (0.1541 nm). For the X-Ray measurements, the step size was 0.065° and the 2 θ scanning range was from 10° to 65°. The data were collected over a period of approximately 25 min with a scan speed of 0.014° s⁻¹.

Scanning electron microscopy (SEM, a Hitachi SU8230 1–30 kV cold field emission gun) was used to investigate the size and shape of the powder crystals and to verify pore formation. Since calcium phosphate minerals have poor electrical conductivity, prior to SEM each sample was coated with a 5 nm thick layer of platinum and then vacuum cleaned for 10 min. By removing the specimen-contamination we aim to minimize the effect of electron beam induced hydrocarbon deposition and to reveal fine surface features [22]. During the imaging of the materials the range of the beam acceleration voltage was between 10 and 15 kV.

For TEM imaging, powder samples were dispersed in ethanol and a drop of the suspension was placed onto a Lacey Carbon Film (Agar Scientific Ltd). Imaging and analysis of the samples was performed with a FEI Titan-cubed, Themis 300 Transmission Electron Microscope (TEM) equipped with multiple HAADF/ADF/BF STEM detectors and a FEI Super-X, 4-detector EDX system.

A Simultaneous Thermal Analyzer (PerkinElmer®, STA 8000) with the capability of acquiring thermogravimetric analysis (TGA) and differential scanning calorimetry (DSC) was used to investigate the reactions and phase changes which take place during the heating of the materials. All thermal experiments were carried out over a temperature range from 30 to 1000 °C and at a heating rate of 20 °C/min.

Nitrogen adsorption/desorption experiments were performed for the determination of the surface area (multi-point BET method), the total pore volume (at P/P₀ = 0.99), and the pore size distribution (BJH method using adsorption data) of the prepared microporous crystals. The materials were firstly outgassed at 150 °C for 16 h under 6.6 × 10⁻⁹ mbar vacuum, using an Automatic Volumetric Sorption Analyzer (Autosorb-1MP, Quantachrome). Measurements were carried out at -196 °C.

The antibacterial activity of the mineral powders was evaluated according to ISO 207043:2007 [20,23]. Bacterial strains of *Escherichia coli* (BL21) and *Bacillus subtilis* were used as the model Gram-negative bacteria while, strains of *Staphylococcus aureus* (ATCC 25923) and *Bacillus cereus* were used as Gram-positive bacteria. Cells were grown in 100 mL of sterile nutrient broth (Luria-Bertani broth, LB) at 150 rpm and 37 °C. They were collected at the

logarithmic stage of growth and the concentration of the suspensions was adjusted to OD600 (optical density at 600 nm) value of 0.5 in 25 mM phosphate buffered saline solution (PBS, Sigma) before incubation with the respective powder sample. Each mineral (before and after drug loading) was tested for three different concentrations namely 25, 50 and 100 µg/mL. After 24 h we measured the absorbance values at OD600 in triplicates and we obtained the mean value for the reported data (average values ±SD).

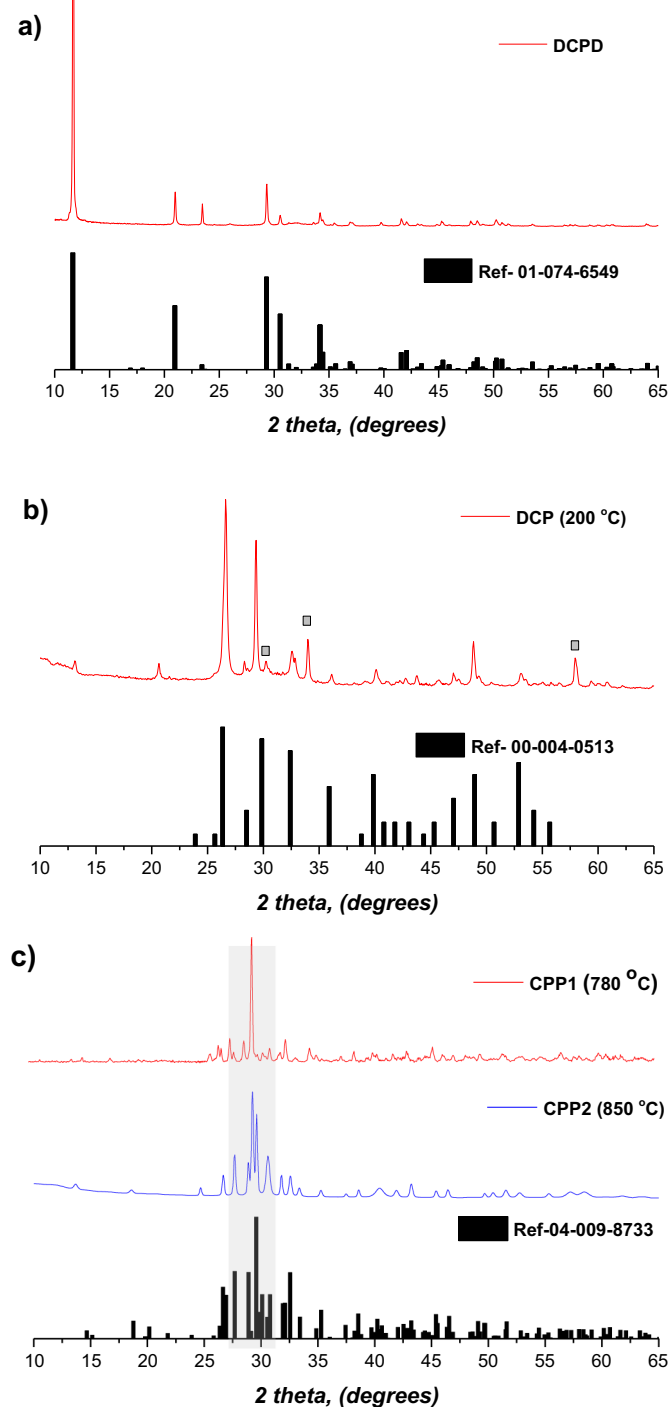
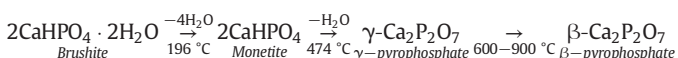


Fig. 2. X-Ray diffraction patterns of the a) initial brushite; b) monetite obtained after heating brushite at 200 °C for 2 h (with the peaks that do not match the reference pattern); c) β -pyrophosphate minerals obtained after heating brushite at two different temperatures (780 °C and 850 °C).

3. Results

In Fig. 1 the characteristic thermogravimetric curve of brushite (DCPD) for a temperature range between 30 and 1000 °C is presented. As expected, three thermal incidents are identified that correspond to the well documented phase transformations of the mineral [24]. The first occurs at 196 °C when DCPD loses two molecules of water and transforms into monetite (CaHPO_4 ; DCP). At 474 °C, DCP loses $\frac{1}{2}$ H_2O and the formation of γ -pyrophosphate ($\gamma\text{-Ca}_2\text{P}_2\text{O}_7$) takes place. Up to this point the initial mass of the mineral is reduced by 25% due to water removal and then remains stable at higher temperatures. In general, pyrophosphates are compounds with dichromate structure and depending on the firing temperature exist in three different forms (Bian et al., 2004). γ -pyrophosphate is transformed to the beta form ($\beta\text{-Ca}_2\text{P}_2\text{O}_7$; CPP) after heating in a broad range of temperatures (between 600 and 900 °C). As we demonstrated in a previous work [18], the transformation into α -pyrophosphate occurs at 1293 °C after which the mineral melts at 1380 °C.



In Fig. 2a the powder diffraction pattern of the initial mineral, DCPD is presented. The peaks from the obtained pattern match the reference XRD data for brushite (01-074-6549) and this is the only detectable phase. The intensity of the measured peaks at $2\theta = 11.56$ and $2\theta = 23.51$ is much higher than these predicted from the reference pattern. Since both these peaks are parallel to the (0 1 0) plane, we can assume

that the different intensity is due to texture of the crystals and that the (0 1 0) plane is the preferred habit of the brushite powder. In Fig. 2b the pattern for the material (DCP) heated at 200 °C is compared with the reference data for monetite and all the characteristic peaks are identified (e.g. at $2\theta = 26.6$, 29.3 and 32.6). In Fig. 2c the two minerals produced by heating DCPD at 780 °C (CPP1) and 850 °C (CPP2) respectively, are compared with the reference pattern of β -pyrophosphate (04-009-8733). In both cases we can match all the peaks with the reference and consequently both materials can be considered as $\beta\text{-Ca}_2\text{P}_2\text{O}_7$. The only difference between the two patterns is the relative intensity of the peak at $2\theta = 29^\circ$ which is much higher for the CPP1 mineral. As discussed before for brushite, the higher intensity can be attributed to texture and preferential growth of the crystals. Heating at higher temperature results in the reordering of the pyrophosphate crystals and texture loss.

In Fig. 3, SEM images of the initial material and the products of heat treatment are presented. As depicted in Fig. 3a, the brushite crystals grow in the shape of 40 μm long platelets with thickness around 1 μm . High magnification images show a homogenous surface without any indications of porosity. After heat treatment at 200 °C and the transformation of brushite to monetite, there is strong evidence that the crystals retain their general platelet shape. The loss of water of crystallisation during the transition from brushite ($\text{CaHPO}_4 \cdot 2\text{H}_2\text{O}$) to monetite (CaHPO_4) is manifested in the appearance of nano-pores and micro-structures (Fig. 3b) as a result of molar volume change. The morphological change of the surface is more apparent for CPP1 (produced by heating brushite at 780 °C) where, extended porosity was identified (Fig. 3c). In this case, the

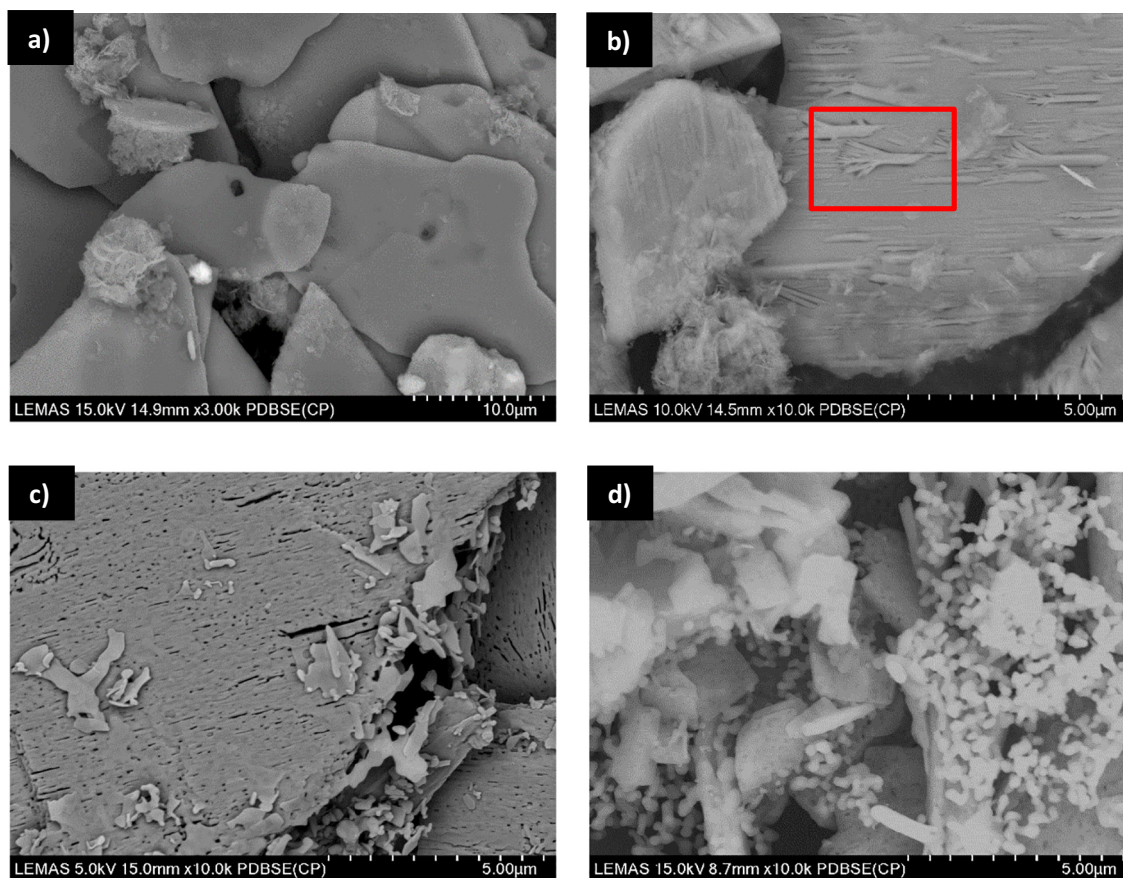


Fig. 3. SEM images of the different minerals tested; a) initial brushite (DCPD); b) monetite crystals (DCP) and nano-structures at the surface (in the red square); c) pyrophosphate obtained after heating brushite at 780 °C (CPP1); d) pyrophosphate obtained after heating brushite at 850 °C for 5 h.

Table 2

Porosimetry results for initial brushite (DCPD), monetite (DCP) and β -pyrophosphate (CPP1).

	DCPD	DCP	CPP1
BET surface area, m ² /g	11.8	27.8	13.2
Micro-pore area, m ² /g	0	1.85	2.59
Pore size, nm	–	10	65

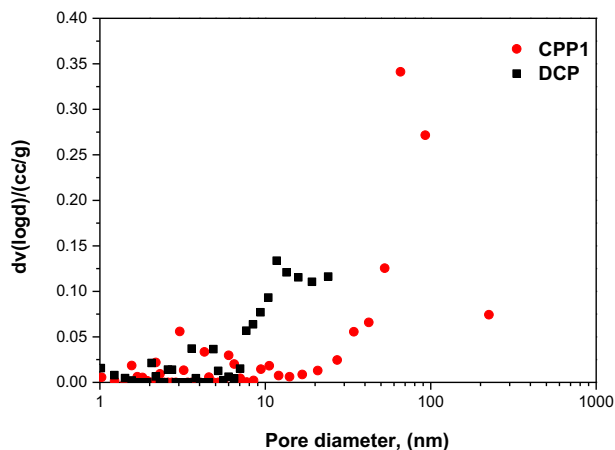


Fig. 4. Pore diameter distribution of pyrophosphate (CPP1) and monetite (DCP) as measured using gas adsorption porosimetry.

pores become larger in size due to the radical volume change between β -pyrophosphate and monetite and because of the reordering and remineralisation of the pyrophosphate crystals. Prolonged heat treatment above 780 °C (e.g. 850 °C for 5 h), changes completely the morphology of the crystals and results in the formation of smaller nuclei along the edge of the parent mineral (Fig. 3d). In this case we can assume that the surface porosity is reduced and thus no drug loading experiments have been performed for this material.

The initial brushite (DCPD) and the heat treatment products DCP and CPP1, were tested with gas adsorption porosimetry to verify the increased porosity which is apparent in the SEM images. As is presented in Table 2, the BET surface area for the initial DCPD was measured at 11.8 m²/g (also Fig. S1). Taking into account the micro pore volume and the micro-pore area were measured to be negligible, we can assume

that this overall value corresponds to the external surface area of the crystals. For the case of DCP the BET surface area is dramatically increased to 27.8 m²/g, with 1.85 m²/g of micro-pore area and the rest the external surface area of monetite crystals. Although the crystals size and shape remain the same during the transformation of brushite to monetite, the increase of the external surface area is attributed to the microstructures that are seen to emerge on the surface of the monetite crystals (Fig. 3b). As these structures are seen to reduce in frequency during the transformation of monetite to pyrophosphate, the total BET surface area for the latter decreases to 13.2 m²/g. CPP1 however presents the highest micro-pore area (2.59 m²/g) with an average pore diameter centred around 65 nm (Fig. 4).

Drug loading experiments were performed utilising chloramphenicol (CAM). As explained above the concentration of CAM in aqueous solutions was determined using UV–VIS spectroscopy, by characterising the intensity of the peak at 275 nm. Before the drug loading experiments, eight control solutions with concentrations in the range of 1 to 150 ppm were tested to obtain a calibration curve that links absorption at 275 nm with the drug's concentration in an aqueous solution (Fig. S2) (based on the Lambert-Beer law). The drug loading percentage at different drug loading periods ($0 < t \leq 168$ h), was calculated according to Eq. (1) and the results for each material incubated over a period of 168 h, and are presented in Fig. 5a.

$$\text{Drug loading\%} = \frac{\text{Drug conc.} (t = 0) - \text{Drug conc.} (t = x)}{\text{Drug conc.} (t = 0)} \times 100 \quad (1)$$

In the case of DCPD (brushite) it was found that practically no drug is loaded on the crystals. Similar results were obtained for DCP (monetite) for which it was estimated that only 1.4% of the initial drug quantity was associated with the mineral. However, in the case of CPP1 (β -pyrophosphate) the percentage of the loaded drug is increased dramatically to 8.5% over a total period of 168 h. As shown in Fig. 5a the loaded quantity over time follows a mono exponential model. After 72 h, 6.2% of the initial drug was already loaded on the CPP1 crystals and a plateau is reached after 144 h (8.3% loaded drug). In order to get an insight into the drug release profile from CPP1 crystals, the cumulative drug release of Doxycycline over a period of 48 h has been monitored by UV-VIS. As is presented in Fig. 5b almost 80% of the loaded drug is released after 48 h (the corresponding drug loading curve is shown in Fig. S3).

In Fig. 6 the FTIR spectra of the drug (chloramphenicol) and the drug-loaded minerals are compared. For chloramphenicol, the vibrational peak of C=O appears at 1683 cm⁻¹ and the peak at 1562 cm⁻¹ is assigned to the N–H bend. The peak at 1518 cm⁻¹ is assigned to NO₂ asymmetric stretch and the broad band at 1411 cm⁻¹ corresponds

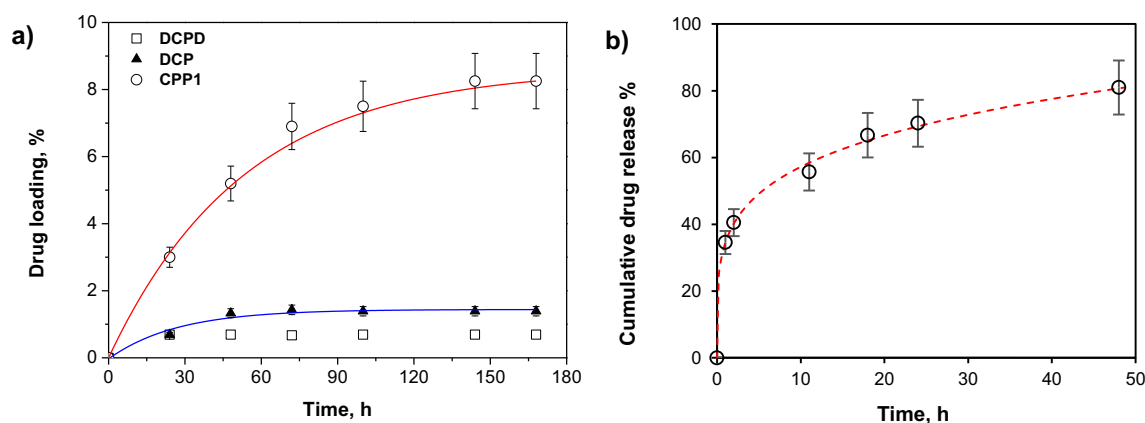


Fig. 5. a) Percentage of loaded drug for three different minerals. Fitting with mono exponential model for only CPP1 and DCP (error bars 10%); b) Release profile of Doxycycline from drug loaded pyrophosphate (D-CPP1). Fitting with a power law model (error bars 10%).

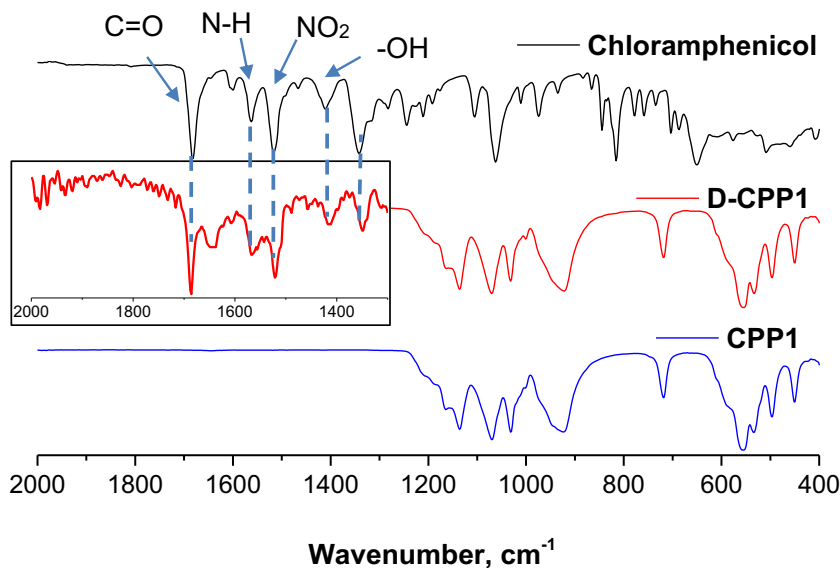


Fig. 6. FTIR spectra of chloramphenicol, the drug loaded and initial minerals D-CPP1 and CPP1. Magnified spectra for D-CPP1 at wavenumbers between 1300 and 2000 cm^{-1} .

to O—H bending. The peaks identified at 1064 and 813 cm^{-1} are assigned to aromatic C—H bends [25]. In order to confirm the loading of the drug to the minerals, we tried to identify the aforementioned peaks in the spectra of D-CPP1, D-DCP and D-DCPD. Pyrophosphate peaks (due to PO_4^{3-} and $\text{P}_2\text{O}_7^{4-}$ ions) appear at wavenumbers between 1150 and 450 cm^{-1} and overlap with several peaks of chloramphenicol. In the 1300 and 1800 cm^{-1} wavenumber range, where no peaks of pyrophosphate are expected, six characteristic peaks of the drug were identified at 1685, 1604, 1568, 1519, 1409 and 1348 cm^{-1} , thereby verifying the presence of chloramphenicol in pyrophosphate crystals. In the cases of D-DCP (drug loaded monetite) and D-DCPD (drug loaded brushite) no FTIR vibrational drug peaks were identified for chloramphenicol (Fig. S4).

To further confirm the presence of the drug on pyrophosphate crystals, the CPP1 and D-CPP1 minerals were analysed by Transmission Electron Microscopy (TEM) (Fig. 7). Chlorine was used as a marker to identify the drug during EDX mapping since chloramphenicol contains two Cl atoms in its molecule ($\text{C}_{11}\text{H}_{12}\text{Cl}_2\text{N}_2\text{O}_5$) and Cl is not involved at any stage of the mineral synthesis. As is presented in Fig. 7a, the projected image of the initial CPP1 crystal shows the presence of 60–100 nm diameter pores running through the crystal which is in agreement with the findings of SEM imaging (Fig. 3c) and gas adsorption porosimetry (Fig. 4). As expected for this material no evidence of Cl was found by EDX. In the case of D-CPP1, Cl is identified both in elemental maps (Fig. 7b) and in area spectra (Fig. 7c) and thus it is confirmed that the crystals are loaded with the drug. Even at higher magnification imaging it wasn't possible to identify any chloramphenicol molecules on the surface of the crystals and that suggests that the drug might have been encapsulated within the pores of the mineral.

The antibacterial properties of the minerals D-CPP1, CPP1, D-DPC and DPC have been evaluated after experiments with four common bacteria. As depicted in Fig. 8a, the drug loaded pyrophosphate (D-CPP1) results in significantly higher inhibition of the bacterial growth than the initial material (CPP1), particularly for the cases of *E. coli* (74% for D-CPP1 and 40% for CPP1) and *B. cereus* (35% for D-CPP1 and 18% for CPP1). For monetite, the drug loaded (D-DPC) and initial mineral (DPC) demonstrated similar effect on bacterial growth and the only statistically significant difference were observed for the case of *E. coli* (37% for D-DPC and 28.5% for DPC) (Fig. 8b).

4. Discussion

Porous pyrophosphate crystals have been formed by heating brushite at 780 °C for 2 h. Although the porosity of the initial material is negligible, the crystals that have been obtained after heating, have a micro-pore area of 2.59 m^2/g and an average pore diameter of 65 nm (Table 2). Pore formation is the result of; a) the removal of water molecules from the brushite crystal structure; b) the reordering and remineralisation into pyrophosphate crystals (above 600 °C). The first phase transformation of brushite occurs at 196 °C when it loses two water molecules and monetite is formed. The initial platelet like shape is retained but the evolution of water results in the appearance of nano-structures on the surface of monetite crystals and consequently there is an increase of the external surface area (Fig. 3). Although there is a dramatic increase of the total BET surface area, from 11.8 m^2/g (value for brushite) to 27.8 m^2/g (value for monetite), the micro-pore surface area, which is important for drug encapsulation, is only 1.87 m^2/g (Table 2). In the case of β -pyrophosphate though, the formation of porosity is a matter of crystal reordering and remineralisation. As identified by thermogravimetric analysis of brushite, the formation of β -pyrophosphate takes place in a broad range of temperatures between 600 and 900 °C (Fig. 1). Depending on the temperature and the duration of heat treatment, the extent of crystal reordering is different and consequently the surface area and the pore distribution vary. As an example, in Fig. 9, the SEM images of pyrophosphate crystals obtained at different temperature and heating times are compared. By increasing the heat treatment temperature, from 780 °C (Fig. 9a) to 850 °C (Fig. 9b), it appears that the number of pores on the surface of the crystals is increased dramatically (heating time for both cases is 2 h). On the other hand, an increase in the heating time, from 2 h (Fig. 9b) to 6 h (Fig. 9c), results in the breakdown of the large platelet like crystals and the formation of nano-crystals which are assumed to have negligible surface or micro-porosity. These three examples are indicative of the potential for controlling the micro-porosity in the resulting mineral phase and consequently the drug loading capacity and potential drug release rate of the mineral system. Depending on the needs of the final application the appropriate drug delivery system can be designed and formulated by controlling the heat treatment conditions of brushite.

Although there is not much difference between the measured micro-pore area of monetite (1.87 m^2/g for DCP) and that of β -pyrophosphate (2.59 m^2/g for CPP1), the quantity of the loaded drug on the second case

is much higher. This behaviour is attributed to the apparent large difference in the average pore size in the two minerals (centred around 10 nm for DCP and 65 nm for CPP1) since the drug loading procedure followed in this work is based on the adsorption of the dissolved drug onto the mineral particles.

The presence of loaded drug into the matrix of pyrophosphate crystals is evident after experiments with four common bacteria. As depicted in Fig. 8a, the drug loaded material (D-CPP1) has enhanced antibacterial activity over *E. coli*, *B. cereus* and *S. aureus* while, for *B. subtilis* there wasn't any significant difference between the effect of D-CPP1 and CPP1. These results are reasonable if we consider that the minimum required concentration of chloramphenicol to inhibit bacteria growth, is only 0.015 $\mu\text{g}/\text{mL}$ for *E. coli* [26], and 14 $\mu\text{g}/\text{mL}$ for *B. subtilis* [27]. In

the case of monetite although there is a trend that indicates better antibacterial behaviour of the drug loaded mineral (D-DCP) this is not statistically significant and could be the result of residual drug on the surface of the crystals. In previous works, β -pyrophosphate proved a suitable biomaterial for dental related applications based on its similarity with dental enamel [11] (in terms of mechanical properties and stability in the acidic environment of oral cavity) and its significant role in the remineralisation of hard tissues [15].

5. Conclusion

In this work we investigated the potential use of β -pyrophosphate as a localised drug delivery system. Porous pyrophosphate crystals have

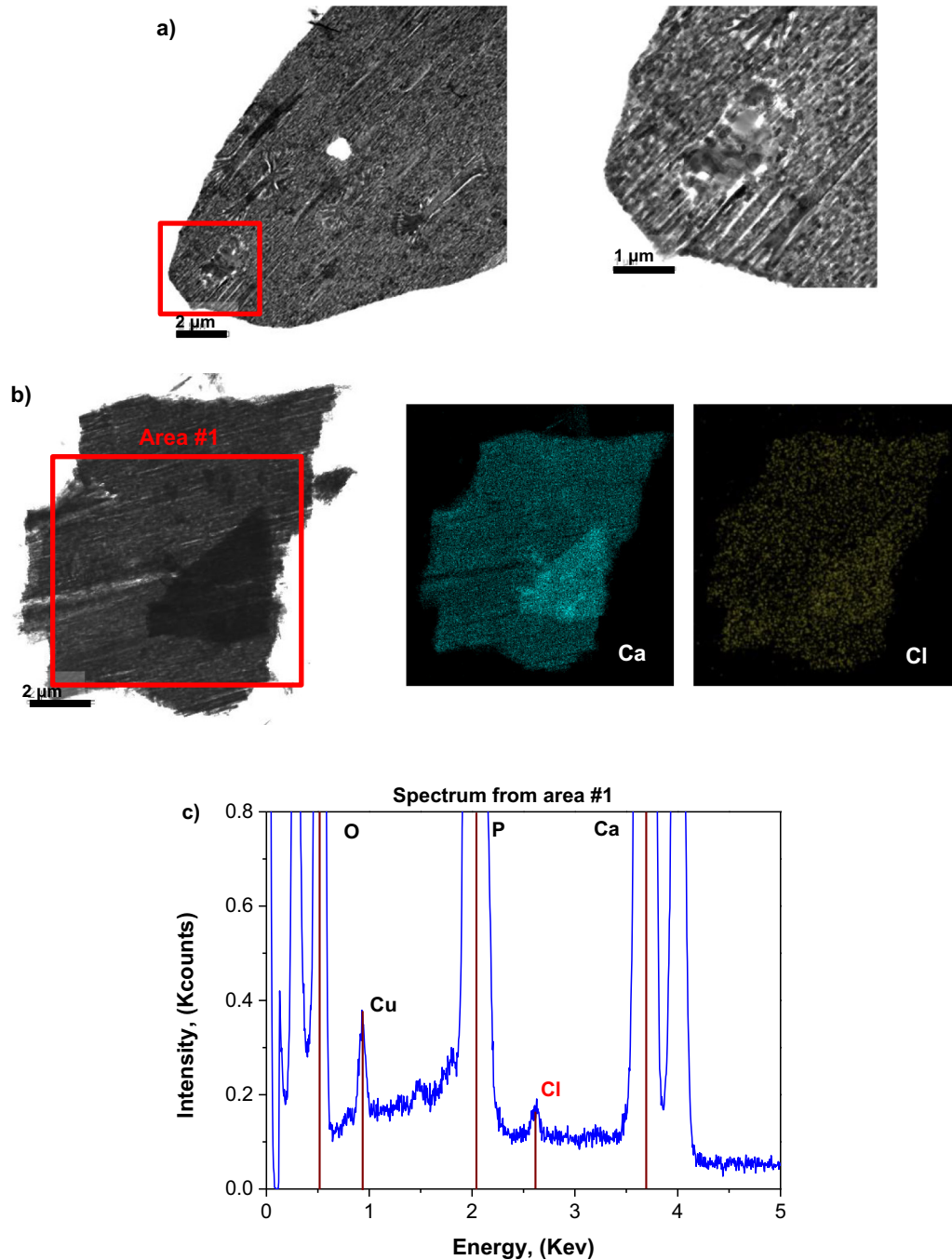


Fig. 7. TEM images and EDX analysis of pyrophosphate crystals before and after drug loading; a) TEM images of the initial CPP1 crystals; b) TEM image of the drug loaded pyrophosphate crystals (D-CPP1) and EDX maps for Ca and Cl; c) EDX spectrum of the drug loaded crystals and identification of the Cl peak at 2.6 KeV (the spectrum of CPP1 is presented in Fig. S5).

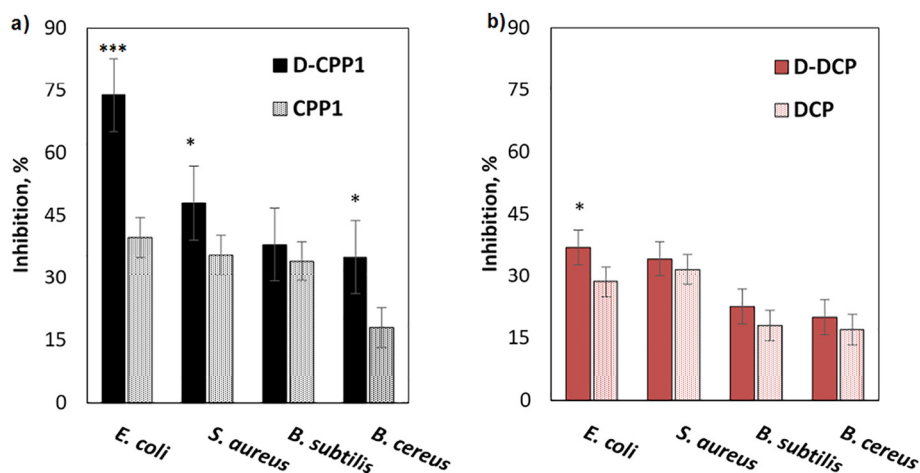


Fig. 8. Effect of drug loaded and initial minerals on the growth of four common bacteria; a) Pyrophosphate (CPP1) and drug loaded pyrophosphate (D-CPP1) crystals (100 $\mu\text{g}/\text{mL}$); b) Monetite (DCP) and drug loaded monetite (D-DCP) crystals (100 $\mu\text{g}/\text{mL}$). *Significant statistical difference between the drug loaded and the initial β -pyrophosphate by 2 sample *t*-test (* $p < 0.05$, *** $p < 0.001$).

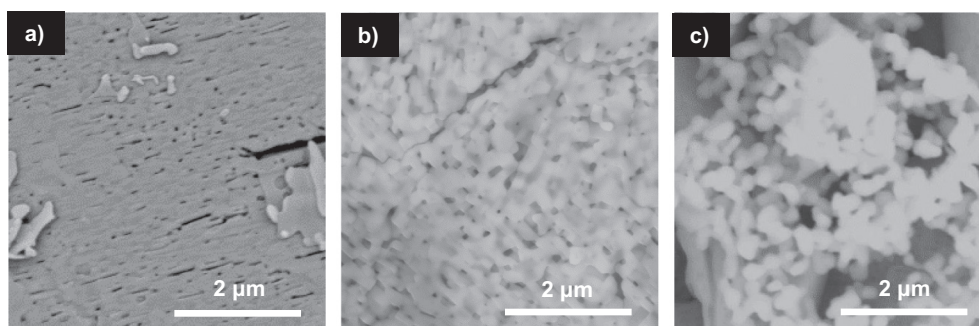


Fig. 9. Surface morphology of pyrophosphate crystals for three different heating conditions; a) 780 $^{\circ}\text{C}$ and 2 h heating time; b) 850 $^{\circ}\text{C}$ and 2 h heating time; c) 850 $^{\circ}\text{C}$ and 6 h heating time.

been obtained by the heat treatment of brushite and a broad spectrum antibiotic, i.e. Chloramphenicol, has been used to demonstrate the drug loading capacity of the resulting mineral. The enhanced antibacterial properties of the drug loaded pyrophosphate have been proven by tests with four common bacteria.

During the transition from brushite to β -pyrophosphate (via intermediate phases of monetite and γ -pyrophosphate) porosity is formed at the surface of the crystals due to; a) water removal from the initial structure; b) break down and reordering of the pyrophosphate crystals. By controlling the conditions of brushite heat treatment (temperature and heating period) it is possible to control the micro-porosity characteristics of the final mineral and consequently to design a suitable drug delivery system based on the demands of each application.

The drug loading potential of β -pyrophosphate in combination with its significant role in hard tissue mineralisation make it a promising material for dealing with significant clinical conditions where bacterial contamination is a critical problem, for example peri-implantitis and periodontitis.

Data availability statement

The raw data required to reproduce these findings cannot be shared at this time as the data also forms part of an ongoing study.

CRediT authorship contribution statement

A.D. Anastasiou: Conceptualization, Funding acquisition, Investigation, Writing - original draft, Writing - review & editing. **M. Nerantzaki:**

Conceptualization, Writing - original draft, Writing - review & editing, Investigation. **A.P. Brown:** Investigation, Writing - original draft, Writing - review & editing. **A. Jha:** Methodology, Project administration, Resources, Writing - original draft, Writing - review & editing. **D.N. Bikiaris:** Methodology, Project administration, Resources, Writing - original draft, Writing - review & editing.

Acknowledgments

The authors acknowledge the sponsors of this work, i) the EU-Marie-Curie-IF Pre-FActo (660147- Recipient A.D. Anastasiou) and ii) Medical Technologies Innovation and Knowledge Centre (phase 2 - Regenerative Devices), funded by the EPSRC under grant number EP/N00941X/1. Also authors would like to acknowledge Dr. K. Triantafyllidis for his kind contribution to the gas adsorption porosimetry experiments. Finally authors would like to acknowledge Mr. John Harrington and Mr. Stuart Micklethwaite for SEM support.

The authors declare that they have no conflict of interest.

Appendix A. Supplementary data

Supplementary data to this article can be found online at <https://doi.org/10.1016/j.matdes.2019.107661> and <https://doi.org/10.5518/568>.

References

- [1] A. Savage, K.A. Eaton, D.R. Moles, I. Needleman, A systematic review of definitions of periodontitis and methods that have been used to identify this disease, *J. Clin. Periodontol.* 36 (2009) 458–467.

- [2] M.P. Cullinan, P.J. Ford, G.J. Seymour, Periodontal disease and systemic health: current status, *Aust. Dent. J.* 54 (2009) (S62-S9).
- [3] E.M. Varoni, S. Vijayakumar, E. Canciani, A. Cochis, L.D. Nardo, G. Lodi, et al., Chitosan-based trilayer scaffold for multitissue periodontal regeneration, *J. Dent. Res.* (2018) (0:0022034517736255).
- [4] F. Sgolastra, M. Severino, R. Gatto, A. Monaco, Effectiveness of diode laser as adjunctive therapy to scaling root planning in the treatment of chronic periodontitis: a meta-analysis, *Lasers Med. Sci.* 28 (2013) 1393–1402.
- [5] X. Chen, G. Wu, Z. Feng, Y. Dong, W. Zhou, B. Li, et al., Advanced biomaterials and their potential applications in the treatment of periodontal disease, *Crit. Rev. Biotechnol.* 36 (2016) 760–775.
- [6] J. Prathapachandran, N. Suresh, Management of peri-implantitis, *Dent. Res. J.* 9 (2012) 516–521.
- [7] C.T. Johnson, A.J. García, Scaffold-based anti-infection strategies in bone repair, *Ann. Biomed. Eng.* 43 (2015) 515–528.
- [8] A. Shayganpour, A. Rebaudi, P. Cortella, A. Diaspro, M. Salerno, Electrochemical coating of dental implants with anodic porous titania for enhanced osteointegration, *Beilstein J. Nanotechnol.* 6 (2015) 2183–2192.
- [9] M.-Z. Yao, M.-Y. Huang-Fu, H.-N. Liu, X.-R. Wang, X. Sheng, J.-Q. Gao, Fabrication and characterization of drug-loaded nano-hydroxyapatite/polyamide 66 scaffolds modified with carbon nanotubes and silk fibroin, *Int. J. Nanomedicine* 11 (2016) 6181–6194.
- [10] S.B. Thorat, A. Diaspro, M. Salerno, In vitro investigation of coupling-agent-free dental restorative composite based on nano-porous alumina fillers, *J. Dent.* 42 (2014) 279–286.
- [11] X. Ge, Y. Leng, C. Bao, S.L. Xu, R. Wang, F. Ren, Antibacterial coatings of fluoridated hydroxyapatite for percutaneous implants, *J. Biomed. Mater. Res. A* 95A (2010) 588–599.
- [12] D. Wiedmer, C. Cui, F. Weber, F.C. Petersen, H. Tiainen, Antibacterial surface coating for bone scaffolds based on the dark catalytic effect of titanium dioxide, *ACS Appl. Mater. Interfaces* 10 (2018) 35784–35793.
- [13] D. Gopi, S. Ramya, D. Rajeswari, P. Karthikeyan, L. Kavitha, Strontium, cerium co-substituted hydroxyapatite nanoparticles: synthesis, characterization, antibacterial activity towards prokaryotic strains and in vitro studies, *Colloids Surf. A Physicochem. Eng. Asp.* 451 (2014) 172–180.
- [14] V. Stanić, A.S. Radosavljević-Mihajlović, V. Živković-Radovanović, B. Nastasijević, M. Marinović-Cincović, J.P. Marković, et al., Synthesis, structural characterisation and antibacterial activity of Ag⁺-doped fluorapatite nanomaterials prepared by neutralization method, *Appl. Surf. Sci.* 337 (2015) 72–80.
- [15] L.M. Grover, A.J. Wright, U. Gbureck, A. Bolarinwa, J. Song, Y. Liu, et al., The effect of amorphous pyrophosphate on calcium phosphate cement resorption and bone generation, *Biomaterials* 34 (2013) 6631–6637.
- [16] K.S. Lee, H.S. Han, Y.C. Kim, J.H. Lo Han, R.H. Seung, H.S. Lee, et al., Evaluation of porous β -calcium pyrophosphate as bioresorbable bone graft substitute material, *Mater. Res. Innov.* 19 (2015) 86–90.
- [17] S.M. Naga, M. Awaad, H.F. El-Maghraby, A.M. El-Kady, Biological performance of calcium pyrophosphate-coated porous alumina scaffolds, *Int. J. Appl. Ceram. Technol.* 11 (2014) 1–11.
- [18] A.D. Anastasiou, S. Strafford, O. Posada-Estefan, C.L. Thomson, S.A. Hussain, T.J. Edwards, et al., β -pyrophosphate: a potential biomaterial for dental applications, *Mater. Sci. Eng. C* 75 (2017) 885–894.
- [19] A.D. Anastasiou, C.L. Thomson, S.A. Hussain, T.J. Edwards, S. Strafford, M. Malinowski, et al., Sintering of calcium phosphates with a femtosecond pulsed laser for hard tissue engineering, *Mater. Des.* 101 (2016) 346–354.
- [20] M. Nerantzaki, N. Kehagias, A. Francone, A. Fernández, C.M. Sotomayor Torres, R. Papi, et al., Design of a multifunctional nanoengineered PLLA surface by maximizing the synergies between biochemical and surface design bactericidal effects, *ACS Omega* 3 (2018) 1509–1521.
- [21] S. Srinath, Management of Periodontal Disease With Doxycycline: An Update, 2015.
- [22] C. Soong, P. Woo, D. Hoyle, Contamination cleaning of TEM/SEM samples with the ZONE cleaner, *Microsc. Today* 20 (2012) 44–48.
- [23] D. Varna, G. Psomas, T. Choli-Papadopoulou, R. Papi, A.G. Hatzidimitriou, P. Aslanidis, Dinuclear copper(I) complexes of N-methylbenzothiazole-2-thione: synthesis, structures, antibacterial activity and DNA interaction, *J. Coord. Chem.* 69 (2016) 2500–2513.
- [24] J.C. Elliott, Chapter 1 - general chemistry of the calcium orthophosphates, in: J.C. Elliott (Ed.), *Studies in Inorganic Chemistry*, Elsevier 1994, pp. 1–62.
- [25] D. Sajan, G.D. Sockalingum, M. Manfait, I.H. Joe, V.S. Jayakumar, NIR-FT Raman, FT-IR and surface-enhanced Raman scattering spectra, with theoretical simulations on chloramphenicol, *J. Raman Spectrosc.* 39 (2008) 1772–1783.
- [26] G. Özek, T. Özek, G. Işcan, K.H.C. Başer, E. Hamzaoglu, A. Duran, Comparison of hydrodistillation and microdistillation methods for the analysis of fruit volatiles of *Prangos pabularia* Lindl., and evaluation of its antimicrobial activity, *S. Afr. J. Bot.* 73 (2007) 563–569.
- [27] M.B. Ningappa, B.L. Dhananjaya, R. Dinesha, R. Harsha, L. Srinivas, Potent antibacterial property of APC protein from curry leaves (*Murraya koenigii* L.), *Food Chem.* 118 (2010) 747–750.